Journal of Southeast University (English Edition)　Vol. 42, No. 1, pp. 1-11　　Mar. 2026　ISSN 1003-7985

Reconstruction of bridge-sensor data and detection of structural damage based on gradient-coupled autoencoder and fully connected network

DUAN Yuanfeng, DING Pengyao, DUAN Zhengteng, CHENG J. J. Roger

(College of Civil Engineering and Architecture, Zhejiang University, Hangzhou 310058, China)

Abstract: A dual-task parallel machine learning framework was developed by integrating a convolutional autoencoder (CAE) and a fully connected neural network (FCNN) via the gradient-coupled mechanism, enabling simultaneous data compression-reconstruction and structural damage identification. Under the condition where 40% of the sensor nodes are missing, the model successfully reconstructs the full sensor network with an R^2 of 0. 916 and normalized root mean square error (NRMSE) of 0. 028 8. Even under significant noise contamination with an SNR of 12 dB, the model maintains strong reconstruction performance, achieving a R^2 of 0. 910 and NRMSE of 0. 025 3. Forty-six structural damage scenarios were simulated using the scaled bridge model. The accuracy of spatial localization and quantification of the damage severity using the framework exceeds 99. 3%. The proposed framework reduces the training time by 54. 4% and iteration counts by 45. 5% compared to conventional two-stage machine learning approaches, demonstrating the efficiency of gradient-coupled optimization.

Key words: structural health monitoring; machine learning; data compression; damage identification; convolutional neural network; fully connected neural network; gradient-coupled mechanism

DOI: 10. 3969/j. issn. 1003-7985. 2026. 01. 001

As a critical component of modern transportation networks, bridges hold irreplaceable strategic value in facilitating regional economic development and optimizing the allocation of societal resources. These infrastructures are consistently exposed to complex geographical environments and are subjected to multifaceted natural hazards, including floods, intense winds, earthquakes, erosion, accidental collisions, and landslides. To ensure lifecycle safety, multi-sensor, fusion-based structural health monitoring (SHM) technologies have become a prevailing choice in engineering practice[1-3]. Through dynamic monitoring of structural responses and environmental parameters, prediction of the structural response, automatic detection of anomalies, and early diagnosis of performance degradation can be achieved, thereby providing supporting data for precision maintenance[4-5].

With the evolution of technology, the development of modern SHM systems is progressing toward high-density sensor networks, with typical cases now integrating hundreds of sensor nodes[6-8]. Although this technological advancement improves the monitoring accuracy, it also leads to a surge in the daily data volume to the terabyte level, causing data storage costs to spike, thereby significantly reducing the real-time transmission and computational efficiency of the system, consequently creating obstacles for identifying structural damage and assessing abnormal states. To overcome this application bottleneck, researchers have focused on efficient data compression and feature extraction by utilizing the features formed by these compressed data encodings to identify structural damage and assess abnormal states. Zhao et al. [9] used principal component analysis (PCA) to compress and reconstruct traffic data. Zhou et al. [10] proposed a wavelet progressive compression algorithm combined with a virtual grid ring model for eliminating boundary effects, providing new insights into the balance between the storage efficiency and energy consumption of embedded sensor networks. Quer et al. [11] introduced a real-time compression and reconstruction framework for wireless sensor networks, in which compressed sensing and PCA were integrated. This framework estimates the statistical signal characteristics in real-time by employing Bayesian networks, demonstrating strong capability for adapting to complex spatiotemporally correlated signals. Duan et al. [12] proposed a two-stage technique for compressing bridge sensor data and identifying structural damage, in which a convolutional autoencoder and gradient-boosted decision trees were combined in series, achieving promising results using a scaled experimental model. Liu et al. [13] presented a damage identification method based on structural response vectors and support vector machine, combined with PCA for noise reduction, enabling efficient and accurate identification of structural damage to

---

Received 2025-04-11, **Revised** 2025-06-19.

Biography: DUAN Yuanfeng (1977—), male, doctor, professor, ceyfduan@zju. edu. cn.

Foundation items: The National Natural Science Foundation of China (No. 52361165658, U24A20169).

Citation: DUAN Yuanfeng, DING Pengyao, DUAN Zhengteng, et al. Reconstruction of bridge-sensor data and detection of structural damage based on gradient-coupled autoencoder and fully connected network [J]. Journal of Southeast University (English Edition), 2026, 42(1): 1-11. DOI: 10. 3969/j. issn. 1003-7985. 2026. 01. 001.

bridges. Dai et al. [14] established a concrete structure identification strategy based on piezoelectric sensor data, utilizing wavelet packet transform-singular value decomposition (WPT-SVD) and genetic algorithm-optimized backpropagation neural networks (GA-BPNN). This platform can prospectively integrate multiple machine learning methods. With the continuous advancement of deep learning methods, mainstream deep learning models such as convolutional neural networks (CNN) have been increasingly applied in the field of bridge health monitoring. Yang et al. [15] developed a machine learning model that integrates wavelet decomposition with gated recurrent units. The model successfully identified abnormal bearing degradation displacements exceeding 4 mm, providing a data-driven, intelligent solution for monitoring the health of long-span bridge bearings. Shan et al. [16] developed a joint deep learning approach based on CNN and LSTM, in which time-frequency domain features were extracted by combining the mean frequency and energy to enhance the damage characterization capability. Shake-table experiments verified that the joint network outperformed standalone CNN or LSTM in identifying the location and severity of structural damage. Zhang et al. [17] proposed an improved spatiotemporal differential graph convolutional neural network (STDGCNN), which achieved high-precision, automatic damage identification for ancient stone arch bridges. Compared with conventional convolutional networks, this model demonstrated superior performance when applied to monitoring data from Lugou Bridge. Zhang et al. [18] proposed a computer vision-based method for tracking dynamic structural deformation. By combining hierarchical convolutional features and Felzenszwalb's histogram of oriented gradients, they developed the HFF-KCF fusion algorithm, achieving high-precision deformation monitoring without reference points for self-centering frame structures subjected to shaking-table tests. Over 90% of the measured displacements and joint rotations had zero pixel errors.

With the advancement of artificial intelligence, the fields of data compression and damage identification are undergoing a significant transformation from statistical learning methods to the integration of diverse deep learning models. However, existing deep learning approaches still face the following critical challenges: (1) the training efficiency of data compression encoders urgently requires improvement, and (2) the feature encoding process remains decoupled from downstream tasks. To address these issues, an innovative dual-task parallel learning framework based on the GCM is constructed in this study. By integrating a convolutional autoencoder (CAE) with a fully connected neural network (FCNN), this framework establishes parallel networks for data reconstruction and damage identification, achieving simultaneous optimization of the training efficiency and feature encoding adaptability.

1 Gradient-Coupled Autoencoder and FCNN (GCAF)

To address the dual bottlenecks of insufficient robustness to noise in the data compression encoding tasks and the lack of task-oriented feature encoding in existing deep learning methods, this study proposes a dual-task parallel deep learning framework based on the GCM. The framework integrates an adaptive noise adversarial layer (ANAL), a CAE-based data compression-reconstruction module, and an FCNN for identifying structural damage, thereby constructing a GCAF with dual-task synergy. The remaining sections sequentially present an overview of the GCAF model, the structure and operational mechanism of ANAL, and a detailed description of GCM.

1.1 Overview of GCAF

This section introduces the structural details and training data flow for the backbone network of GCAF (Fig. 1), namely the CAE and FCNN for downstream identification of structural damage.

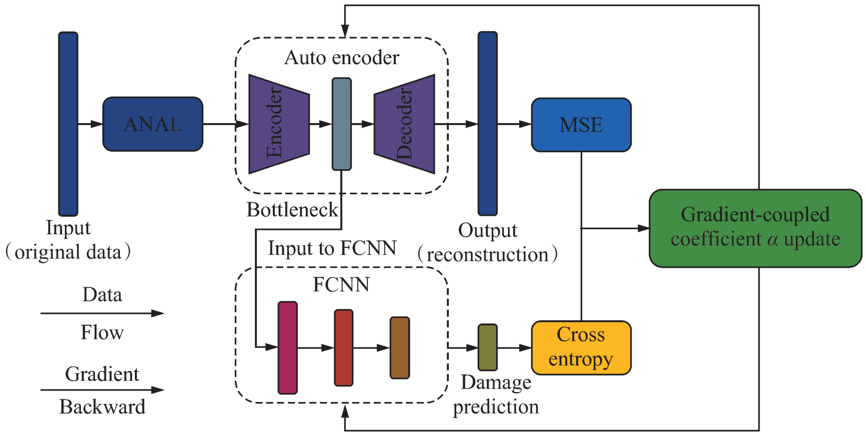

Fig. 1 Topological diagram of GCAF

The CAE consists of a compression encoder and a reconstruction decoder. The encoder comprises 10 convolutional layers that progressively reduce the dimensionality of the input data $\boldsymbol{X}^{5\times 2\,048}$ (where 5 represents the number of sensors and 2 048 denotes the sample length) down to a 4 096-dimensional bottleneck feature. LeakyReLU activation functions are applied between the convolutional layers to enhance the nonlinear feature encoding capability of the model. The decoder employs five transposed convolutional layers to gradually restore the bottleneck features back to the original data matrix dimensions $\boldsymbol{X}'^{5\times 2\,048}$, where the ReLU functions provide nonlinear activation between transposed convolutional layers. The FCNN is constructed by cascading five linear, fully connected layers, and an exponential dimensionality reduction strategy is employed to progressively decrease the bottleneck feature vector from 4 096 dimensions to the specified output dimensions (4 096→2 048→1 024→512 →256→output dimension). LeakyReLU activations are used between fully connected layers, along with a dropout strategy for network regularization. The output of the FCNN represents the probability predictions for each category.

In the training process, the data first pass through the ANAL module for noise injection, and are then subjected to compression and feature encoding using the encoder; this process generates the compressed bottleneck features. These features are simultaneously fed into both the decoder and FCNN. On the one hand, the features are used for data reconstruction, where the resulting output is used as the input for the mean square error function, which calculates the data reconstruction loss L_{comp}. On the other hand, the data undergo structural anomaly identification classification to obtain the damage prediction results, which are then input into the cross entropy function to compute the loss value L_{cls} for the structural anomaly recognition task. Finally, the GCM couples and backpropagates the gradients generated by these two losses with respect to the parameters of both the CAE and FCNN, while simultaneously updating the corresponding gradient coupling coefficient α in the GCM (the significance of the specific parameters and update mechanism are detailed in Section 2). This completes one training iteration.

During the test, the dual-task parallel architecture of the GCAF model simultaneously achieves data compression-reconstruction and structural damage identification through the following core methodological logic. First, the input data are subjected to feature compression via the CAE encoder, thereby generating the bottleneck feature vectors. Subsequently, the CAE decoder reconstructs the sensor data from these compressed features. Concurrently, the FCNN utilizes these feature vectors to perform synchronous damage localization and severity identification.

For damage localization, the GCAF model outputs position-specific damage probability values, enabling precise damage localization. To identify the damage severity, the model generates case-specific probability prediction vectors, where the value of each element determines the exact level of damage severity. This completes the full cycle of damage identification testing in the GCAF framework.

1.2 ANAL

The ANAL proposed in this study establishes a dynamic noise injection paradigm based on a trainable parameter S and an adaptive feature extractor (AFE), where S regulates the amplitude of the generated Gaussian noise, while the AFE produces spatiotemporal feature distribution matrices from the input data to guide noise injection. The AFE comprises two convolutional layers dedicated to extracting spatiotemporal features, outputting a feature distribution matrix with dimensions identical to those of the input data. The ANAL operational workflow consists of three core phases:

(1) The parameter S serves as a control variable that is input to the Gaussian noise generator, producing a white noise base $\boldsymbol{N}^{5\times 2\,048} - \mathrm{N}(0, S^2)$.

(2) The input data $\boldsymbol{X}^{5\times 2\,048}$ is processed through the AFE, and the resulting features are transformed via a Sigmoid function (Eq. (1)) to output a spatiotemporal feature distribution matrix $\boldsymbol{M} \in [0, 1]^{5\times 2\,048}$. This matrix quantitatively characterizes the feature sensitivity at each spatiotemporal position within the input data.

$$\mathrm{Sigmoid}(x) = \frac{1}{1 + \mathrm{e}^{-x}} \tag{1}$$

(3) Feature-guided noise amplitude modulation is achieved through element-wise matrix multiplication (⊙), generating a feature-adaptive noise matrix (Eq. (2)). This result is then additively combined with the input data to complete the noise injection process.

$$\boldsymbol{X}_{\text{noised}} = \boldsymbol{X} + (\boldsymbol{N} \odot \boldsymbol{M}) \tag{2}$$

This architecture overcomes two limitations of conventional noise injection methods: (1) The feature-aware module enables data-driven modeling of the noise sensitivity, eliminating the constraints of manually designed prior distributions that typically result in uniform noise amplitudes and homogeneous spatiotemporal distributions. (2) The dynamic amplitude adjustment mechanism allows the noise intensity to adaptively evolve during the training process, breaking through the limitation of fixed-amplitude artificial noise injection.

1. 3 Gradient-coupled joint mechanism

In conventional frameworks for data compression encoding and structural damage identification tasks, a serialized and independent training paradigm is typically employed for the unsupervised learning of autoencoders and supervised learning of downstream classification tasks. This approach has two fundamental limitations: (1) the encoder parameters remain frozen during the classification phase, leading to significant underutilization of computational resources; (2) the encoded features generated by the decoupled two-stage training process lack task-specific adaptability. To address these limitations, this study proposes an innovative gradient coupling mechanism that enables concurrent data reconstruction and damage detection while permitting backpropagation of classification loss gradients to the encoder, thereby achieving dynamic adaptation between the feature encoding process and classification task requirements. The implementation mechanism operates through the following procedures:

(1) Implement dynamic weight adjustment and gradient-interactive loss functions.

$$L_{\text{total}} = \alpha L_{\text{cls}} + (1 - \alpha) L_{\text{comp}} \tag{3}$$

where L_{total} denotes the total loss function. The gradient coupling coefficient α controls the task balance: as $\alpha \to 1$, the mode prioritizes classification task learning, while $\alpha \to 0$ shifts the focus to compression-reconstruction task learning.

(2) Gradient coupling coefficient initialization. The initial value α_{init}, maximum value $\alpha_{\max}$, and minimum value $\alpha_{\min}$ are configured with the constraint α_{init}, $\alpha_{\max}$, $\alpha_{\min} \in (0, 1)$ to prevent the model from exclusively focusing on either task. This study employs $\alpha_{\text{init}} = 0.5$, $\alpha_{\max} = 0.9$, $\alpha_{\min} = 0.1$.

(3) Classification task performance evaluation window. A sliding window of length 10 is implemented to assess model performance. Every five training iterations, the classification capability of the model is evaluated using the test set, with the F1-score as the metric.

(4) Three-stage α update mechanism. A sliding window of length 10 is used to track the F1-scores, where coefficient update decisions are made every five training epochs.

The regulation process comprises three distinct physical stages, as shown in Fig. 2:

(1) Breakdown stage: Triggered when all monitored F1-scores in the sliding window exceed 0. 95. In this stage, an exponential decay strategy is used to rapidly reduce the coupling intensity, formulated as follows:

$$\alpha(t) = \alpha_0 \exp(-(t - t_0)\gamma) \tag{4}$$

where α_0 and t_0 represent the initial gradient coupling coefficient and epoch number at the onset of the breakdown stage, respectively; γ is the adjustable decay coefficient (set to 0. 1 in this study).

(2) If not all monitored F1-scores in the observation window exceed 0. 95, but the latest five detection results remain above 0. 95, the maintain stage is triggered, keeping the current gradient coupling coefficient constant.

(3) If neither of the aforementioned conditions is met, the warmup stage is triggered by default, performing stepwise parameter updates at a fixed learning rate $\eta = 0.05$ as follows:

$$\alpha_{\text{new}} = \min(\alpha_{\text{old}} + \eta, \alpha_{\max}) \tag{5}$$

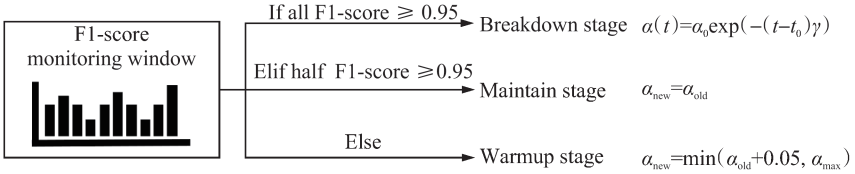

Fig. 2 Three-stage mechanism of updating the gradient coupling coefficient

The "min" function ensures that the gradient coupling coefficient does not exceed the maximum threshold during updates, thereby preventing excessive dominance by any single task learning process.

2 Three-Span Continuous Beam Scaled Experimental Platform

This study employs an experimental scaled continuous beam bridge model (Fig. 3) with three spans (2. 4 m + 4. 0 m + 2. 4 m), totaling 8. 8 m in length. The structure is artificially divided into 44 units, each measuring 20 cm in length and weighing 2. 252 kg. This setup facilitates subsequent sensor installation and structural damage configuration. A No. 10 I-beam conforming to the GB/T 706—2016 standard is used in the cross-section of the main girder, where the direction with lower flexural stiffness is designated as the vertical bending principal axis (Fig. 4). This design strategy achieves two objectives: (1) reducing the vertical bending stiffness of the structure, which significantly lowers the natural vertical vibration frequency of the model, thereby enabling better approximation of the actual dynamic bridge characteristics; (2) effectively suppressing excitation of the lateral vibration modes during experimental loading, thereby ensuring the validity and accuracy of the measurement at the model design level. The bridge features four hinged supports, each constructed to permit rotational freedom while incorporating vertical displacement restraint devices to lock vertical movement, guaranteeing structural stability under vertical loading. The details of the support are illustrated in Fig. 4.

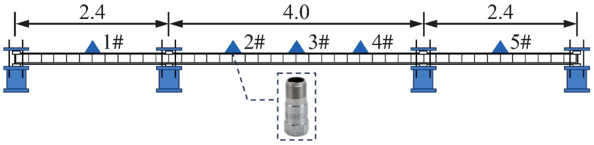

Fig. 3 Layout of experimental model and sensor distribution (unit: m)

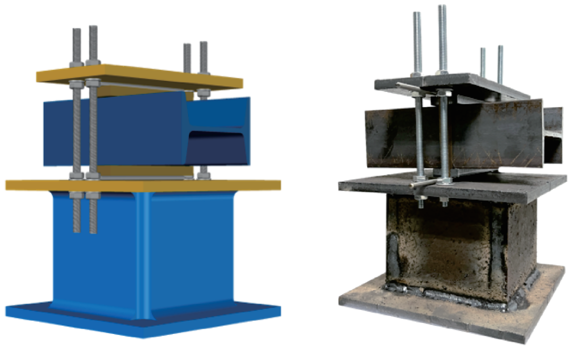

(a) (b)

Fig. 4 CAD model and photograph of the support and pier. (a) Model; (b) Photograph

In this system, a controlled hammer impact loading is used to excite the bridge model. For each test condition, a continuous 64-s valid data segment is selected from the sensor data. A sliding window method is employed for sample segmentation, with a window size of 5 × 2 048 (5 is the number of sensor channels and 2 048 is the number of time-domain data points) and a step size of 256 points is used for window sliding to obtain 500 data samples, which are divided into training and testing sets in a 4∶1 ratio.

To systematically verify the performance of the proposed GCAF model in the dual tasks of data compression-reconstruction and structural damage identification, three different test scenarios were simulated in this experiment.

2.1 Partial sensor network node data missing

The input data from randomly selected sensor nodes is masked (simulating scenarios such as sensor failure or communication interruption), forcing the model to reconstruct the complete sensor network data outputs based solely on observations from remaining nodes. This experimental condition not only verifies the capability of GCAF for modeling the time-domain dynamic characteristics of individual sensors but, more importantly, demonstrates its breakthrough performance and robustness in learning multi-scale physical field coupling relationships.

To address partial node failures in the sensor network, two types of failure conditions were established herein: single-sensor failure and dual-sensor failure. Based on the symmetric distribution characteristics of the sensor network (five sensors arranged symmetrically), nine non-repetitive failure scenarios were designed by eliminating symmetric equivalent conditions (Table 1).

Table 1 Different cases with missing sensor data

Case	Missing sensor	Case	Missing sensors	Case	Missing sensors
SMC1	1#	DMC1	1#, 2#	DMC4	1#, 5#
SMC2	2#	DMC2	1#, 3#	DMC5	2#, 3#
SMC3	3#	DMC3	1#, 4#	DMC6	2#, 4#

Note: SMC represents a case with a single missing sensor; DMC represents a case with two missing sensors.

2.2 Spatial localization of structural damage

Chen et al. [19] demonstrated the rationality of simulating stiffness reduction-type damage by adding mass through analytical analysis of the undamped free vibration dynamic equations of structures. Assuming the element stiffness reduction ratio is ε_K ($0 < \varepsilon_K < 1$), the additional mass ratio of the element is ε_M ($\varepsilon_M > 0$). The specific relationship between these parameters can be expressed as follows:

$$\varepsilon_M = \frac{\varepsilon_K}{1 - \varepsilon_K} \tag{6}$$

This equation indicates dynamic equivalence between the increase in mass and the reduction in stiffness. Thus, the structural damage can be simulated by adding mass. In this study, mass addition is employed to simulate damage scenarios involving stiffness reduction in the structural elements. Such an approach facilitates the efficient and reproducible setup of multiple damage conditions in experiments, eliminating the need for actual damage implementation and effectively reducing experimental costs.

Herein, structural damage is simulated through additional mass loading, employing an NdFeB permanent magnet (neodymium magnet) array with a surface magnetic flux density of 1.2 T for precise positioning and installation. This approach simultaneously avoids increasing the structural stiffness while meeting the requirements for altering the dynamic structural performance.

In the scenarios for spatial localization of the structural damage, a single-unit mass block (2.252 kg) is attached at 19 distinct locations on the bridge model (five locations on each side span and nine locations on the central span, totaling 19 spatial damage localization cases). The specific locations for attachment of the mass are illustrated in Fig. 5.

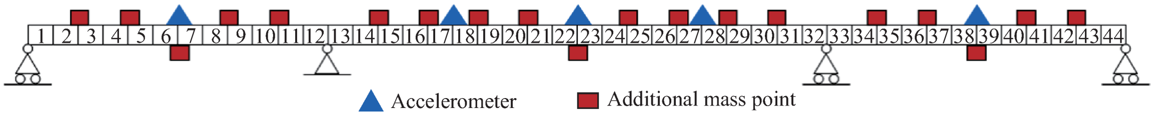

Fig. 5 Map of additional mass points for the structural damage localization task

2.3 Identifying the severity of structural damage

Three-level additional mass loading experiments were conducted at three strategically selected locations for the detection of structural anomalies. The measurement points were established at the near-bearing zone of the side span (Unit 10), mid-span section of the central span (Unit 20), and mid-span section of the side span (Unit 38), as illustrated in Fig. 6. Three graded mass modules were employed: 0.4M (0.901 kg), 0.7M (1.576 kg), and 1.0M (2.252 kg), where M represents the standard unit mass of 2.252 kg. The experimental design was based on two key considerations: first, the sensitivity of the model to weak-signal damage detection was tested by monitoring the change in the characteristic dynamic response of the bearing zone; second, the capability of the model for decoupling and analyzing anomaly features across different longitudinal bridge sections was verified by monitoring the spatial distribution of the mid-span measurement points. The specific additional mass parameters for each damage scenario are detailed in Tables 2 to 4.

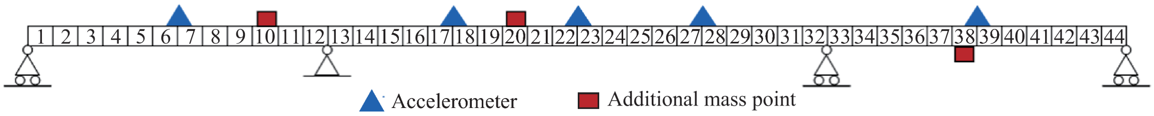

Fig. 6 Map of additional mass points for the damage degree identification task

Table 2 Additional mass distribution of single damage case (SDC) kg

Case	Unit 10	Unit 20	Unit 38	Case	Unit 10	Unit 20	Unit 38	Case	Unit 10	Unit 20	Unit 38
SDC1	0.90	—	—	SDC4	—	0.90	—	SDC7	—	—	0.90
SDC2	1.58	—	—	SDC5	—	1.58	—	SDC8	—	—	1.58
SDC3	2.25	—	—	SDC6	—	2.25	—	SDC9	—	—	2.25

Note: The symbol "—" indicates that no additional mass is added.

Table 3 Additional mass distribution of double damage case (DDC) kg

Case	Unit 10	Unit 20	Unit 38	Case	Unit 10	Unit 20	Unit 38	Case	Unit 10	Unit 20	Unit 38
DDC1	0.90	0.90	—	DDC4	1.58	0.90	—	DDC7	2.25	0.90	—
DDC2	0.90	1.58	—	DDC5	1.58	1.58	—	DDC8	2.25	1.58	—
DDC3	0.90	2.25	—	DDC6	1.58	2.25	—	DDC9	2.25	2.25	—

Note: The symbol "—" indicates that no additional mass is added.

Table 4 Additional mass distribution of triple damage case (TDC) kg

Case	Unit 10	Unit 20	Unit 38	Case	Unit 10	Unit 20	Unit 38	Case	Unit 10	Unit 20	Unit 38
TDC1	0.90	0.90	0.90	TDC4	0.90	1.58	2.25	TDC7	1.58	2.25	0.90
TDC2	1.58	1.58	1.58	TDC5	0.90	2.25	1.58	TDC8	2.25	0.90	1.58
TDC3	2.25	2.25	2.25	TDC6	1.58	0.90	2.25	TDC9	2.25	1.58	0.90

Note: The symbol "—" indicates that no additional mass is added.

To balance the sample sizes across different cases, the tasks are divided into sensor failing, spatial localization of damage, and identification of damage severity, as shown in Table 5. The sensor failure cases include three cases with single missing sensors and six cases with dual missing sensors, totaling nine cases. The side-span dam-

Table 5 Detailed datasets for experimental cases

Task	Case	Sub-case	Training set	Testing set	Total
Reconstruction of missing data	Sensor missing	9	3 600	900	4 500
Spatial location of damage	Mid-span damage	9	3 600	900	4 500
	Side-span damage	10	4 000	1 000	5 000
Identification of damage severity	Single damage	9	3 600	900	4 500
	Double damage	9	3 600	900	4 500
	Triple damage	9	3 600	900	4 500

age cases consist of five sub-cases for each of the left and right side spans, resulting in ten cases.

3 Data Compression and Reconstruction Results

3.1 Data compression and reconstruction results for missing sensor scenarios

Based on the dataset established for the condition in which a sensor is missing (Section 2), this section presents the training and testing of the GCAF, with a focus on evaluating the efficacy of the model for data compression and feature reconstruction. To enhance the training stability and convergence efficiency, the hyperparameter configuration employed in the experimental design is as follows: batch size of 256 samples, Adam optimizer for parameter updates, and initial learning rate of 0.001.

Notably, the dynamic learning rate was adjusted using the ReduceLROnPlateau strategy. Specifically, when the model's test loss failed to show significant improvement over 100 consecutive training epochs, the system automatically reduced the learning rate by applying a decay factor of 0.1. This adaptive mechanism effectively balances the trade-off between the convergence speed and optimization precision during training, ensuring thorough exploration of the parameter space while progressively refining the solution accuracy when approaching optimal regions.

Two distinct phase-transition regions are apparent in the loss function curve, demonstrating significant correlation with the predefined learning rate adjustment strategy, as shown in Fig. 7. When parameter updates become trapped in local optima (corresponding to plateau regions in the curve), the learning rate decay mechanism is triggered, effectively enhancing the efficiency of parameter space exploration. This dynamic regulation process not only highlights the limitations of fixed learning rate strategies in dealing with complex non-convex optimization problems, but more importantly, reveals the practical value of phased learning rate control in improving the generalization capability of deep models.

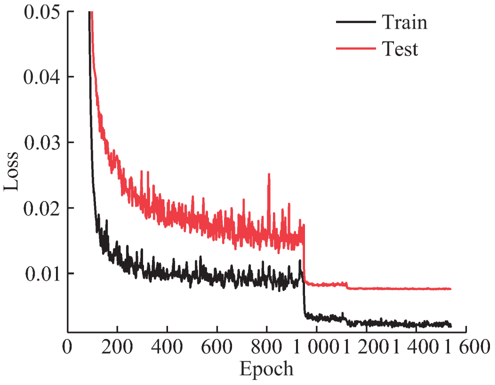

Fig. 7 Loss function curve

Comparative analysis of the reconstructed and original signals (Fig. 8) demonstrates the superior compression-reconstruction capability of the model. For the reconstructed signals, the peak and valley values were excellently fitted, while faithfully reproducing localized minor fluctuations. The scatter distribution between the reconstructed and true signals displays a characteristic spindle shape, indicating that the model tends to generate larger relative errors during minor fluctuation intervals. This error distribution pattern reflects the inherent challenge in capturing subtle signal variations where waveform features become less distinct.

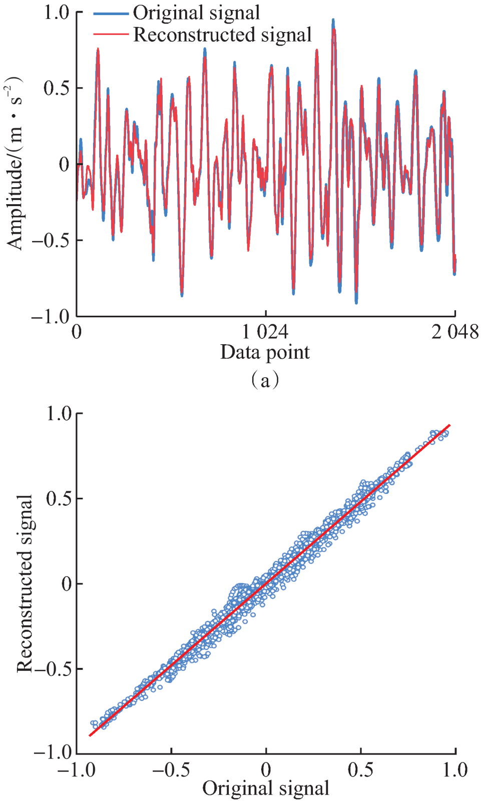

(a)

(b)

Fig. 8 Reconstruction results. (a) Time-domain comparison; (b) Linear fitting

For the nine scenarios with missing sensors, the model performance was evaluated using two complementary metrics: the coefficient of determination (R^2) to characterize the temporal-domain goodness-of-fit between the reconstructed and original signals, and the normalized root mean square error (NRMSE) to assess the global reconstruction error. The dimensionless nature of the NRMSE effectively eliminates evaluation bias caused by amplitude variations across different sensor channels. These two indicators have a mutually validating relationship, where the mathematical expressions are as follows:

$$R^2 = 1 - \frac{\sum_{i=1}^{n} (y_i - \hat{y}_i)^2}{\sum_{i=1}^{n} (y_i - \bar{y})^2} \tag{7}$$

$$\mathrm{NRMSE}=\frac{\sqrt{\frac{1}{n}\sum_{i=1}^{n}(y_i-\hat{y}_i)^2}}{y_{\max}-y_{\min}} \tag{8}$$

where y_i represents the true data value, $\hat{y}_i$ denotes the predicted data value, $\bar{y}$ is the mean of the observed true value data, and n indicates the sample dimension.

Dual-index validation of the set of test samples in the sensor missing scenarios shows that across all nine scenarios (Table 6), the mean R^2 values remained consistently above 0.915, while the mean NRMSE values remained below 0.028 8. For the dual-sensor missing cases specifically, the minimum average R^2 reached 0.916, demonstrating the excellent capability of the model for reconstructing full sensor network data even with 40% of the sensor nodes missing. Notably, this performance was achieved without incorporating any prior knowledge about the location of the missing sensor(s), conclusively verifying the model's powerful feature extraction capability.

Table 6 Data reconstruction indexes for each case

Case	R^2			NRMSE		
	Best	Average	SD	Best	Average	SD
SMC1	0.979	0.928	5.92E−02	1.66E−02	2.32E−02	2.94E−03
SMC2	0.975	0.915	7.45E−02	1.80E−02	2.47E−02	3.32E−03
SMC3	0.980	0.928	6.69E−02	1.64E−02	2.25E−02	2.86E−03
DMC1	0.973	0.916	6.62E−02	2.06E−02	2.88E−02	3.54E−03
DMC2	0.982	0.942	5.43E−02	1.59E−02	2.35E−02	2.50E−03
DMC3	0.984	0.946	5.78E−02	1.64E−02	2.22E−02	2.19E−03
DMC4	0.974	0.920	1.22E−01	1.81E−02	2.74E−02	3.86E−03
DMC5	0.981	0.929	6.57E−02	2.49E−02	1.72E−02	2.84E−03
DMC6	0.979	0.935	5.67E−02	1.76E−02	2.41E−02	2.65E−03

3.2 Compression and reconstruction of noise-affected data

To systematically evaluate the robustness of the GCAF model for addressing noise enhancement, an ablation comparison experimental framework was designed based on ANAL. By constructing a test environment incorporating five noise injection intensity gradients (discretized SNR parameters: 12, 15, 18, 21, and 24 dB), the performance of the model was quantitatively analyzed.

The comparative results (Fig. 9) clearly demonstrate that even under the influence of a noise level at SNR = 12 dB, the model achieved an average performance of R^2 = 0.910 and NRMSE = 0.025 3. Across all noise levels, the mean, median, and standard deviation were significantly improved for both R^2 and NRMSE. The mean R^2 increased by an average of 0.046 across the five noise conditions, whereas the mean NRMSE decreased by an average of 0.011.

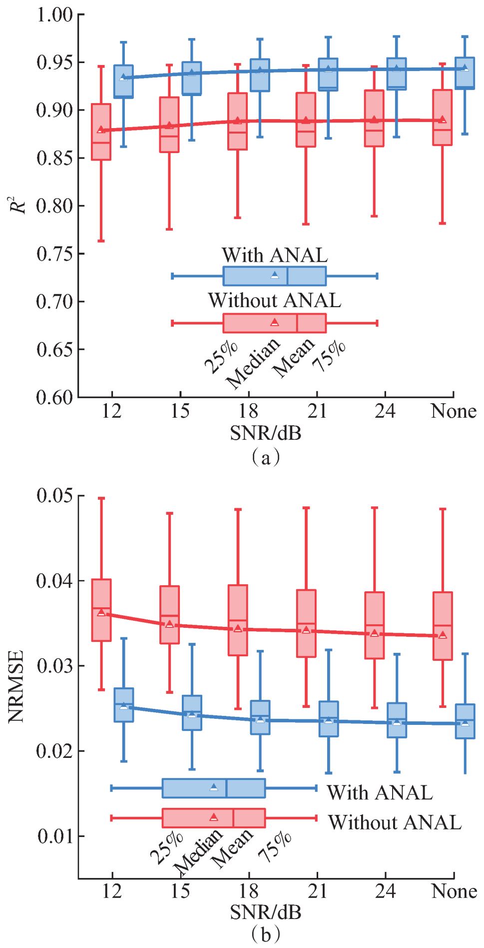

(a)

(b)

Fig. 9 Results demonstrating improved robustness of ANAL for modeling noise. (a) R^2; (b) NRMSE

Notably, the reconstruction performance under noiseless conditions was also significantly enhanced. This indicates that ANAL's noise injection during training functions as an adversarial regularization mechanism. By introducing noise interference, it adversarially challenges the model's feature learning, thereby improving its feature extraction capability.

4 Identification of Structural Damage

4.1 Spatial localization of structural damage

This section evaluates the performance of GCAF in tasks involving the spatial localization of structural damage through a dual-validation mechanism: on the one hand, the capability of the model of localizing spatial damage is assessed using a confusion matrix; on the other hand, the data compression and reconstruction capability of the model are measured via a dual indicator system comprising R^2 and NRMSE, thereby verifying the model's performance in both tasks (Table 7).

The damage identification capability is evaluated using the accuracy (A_{ccu}), aiming to assess the efficacy of the model for damage localization and severity identification, where the specific formula is defined as follows:

Table 7 Data reconstruction results for the structural damage localization task

Statistical metrics	Side-span damage		Mid-span damage	
	R^2	NRMSE	R^2	NRMSE
Best	0.989	1.32E−02	0.983	1.56E−02
Average	0.955	1.97E−02	0.953	2.12E−02
SD	4.85E−03	1.95E−03	5.51E−03	2.93E−03

$$A_{\text{ccu}} = \frac{C}{N} \tag{9}$$

where C represents the number of damaged samples correctly predicted by the model, which is the sum of all elements on the diagonal of the confusion matrix; N represents the total number of samples, which is the sum of all elements in the confusion matrix.

The quantitative analysis based on the confusion matrix (Fig. 10) demonstrates that the model achieved an overall accuracy of 99. 6% in the task of spatially localizing the damage. This not only effectively verifies the strong spatial decoupling capability of the model when confronting structural anomalies but also confirms the feasibility of using additional mass to simulate structural anomalies in scaled experimental models, fully justifying the rationality of the experimental design.

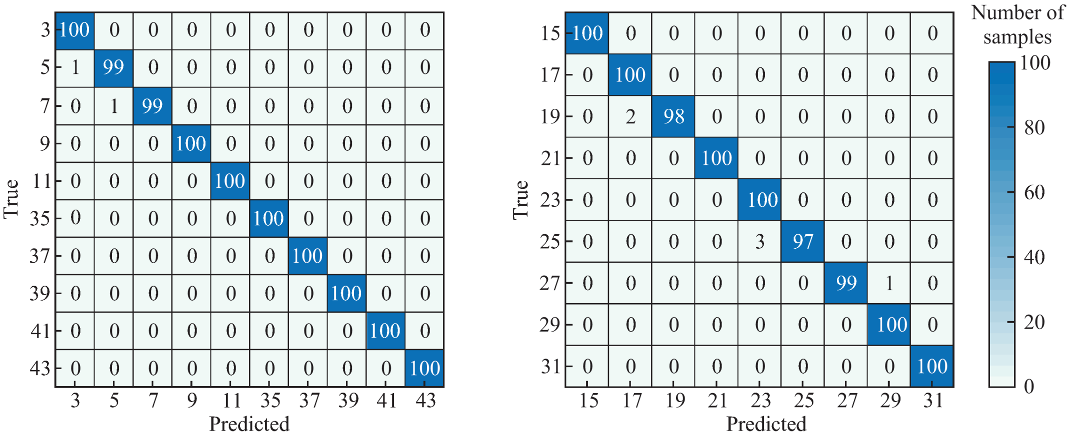

	3	5	7	9	11	35	37	39	41	43
3	100	0	0	0	0	0	0	0	0	0
5	1	99	0	0	0	0	0	0	0	0
7	0	1	99	0	0	0	0	0	0	0
9	0	0	0	100	0	0	0	0	0	0
11	0	0	0	0	100	0	0	0	0	0
35	0	0	0	0	0	100	0	0	0	0
37	0	0	0	0	0	0	100	0	0	0
39	0	0	0	0	0	0	0	100	0	0
41	0	0	0	0	0	0	0	0	100	0
43	0	0	0	0	0	0	0	0	0	100

(a)

	15	17	19	21	23	25	27	29	31
15	100	0	0	0	0	0	0	0	0
17	0	100	0	0	0	0	0	0	0
19	0	2	98	0	0	0	0	0	0
21	0	0	0	100	0	0	0	0	0
23	0	0	0	0	100	0	0	0	0
25	0	0	0	0	3	97	0	0	0
27	0	0	0	0	0	0	99	1	0
29	0	0	0	0	0	0	0	100	0
31	0	0	0	0	0	0	0	0	100

(b)

Fig. 10 Confusion matrix for identifying structural damage. (a) Side-span; (b) Mid-span

The data compression and reconstruction results shown in Table 7 demonstrate that the GCAF model attained average global reconstruction metrics of $R^2 = 0.953$ and NRMSE = 0. 021 2, validating the robust mapping capability of the network's feature space. As indicated by horizontal comparison, the reconstruction metrics for side-span anomaly samples were superior to those of the mid-span anomaly samples. This pattern aligns with the actual physical characteristics of the scaled model, where mid-span anomalies induce significantly greater dynamic response variations compared to equivalent anomalies in side spans, thereby imposing higher demands on the model's feature extraction and mining capabilities.

4. 2 Identification of the severity of structural damage

For identifying the severity of structural damage, quantitative analysis was conducted by following the same methodology as in Section 4. 1. The confusion matrix-based quantitative analysis (Fig. 11) demonstrates that the model achieved an overall accuracy of 99. 3% in identifying the damage severity, with only two misclassified samples in the triple-damage scenario. Based on the results of the data compression and reconstruction analysis (Table 8), the GCAF model attained average global reconstruction metrics of $R^2 = 0.949$ and NRMSE = 0. 021 0.

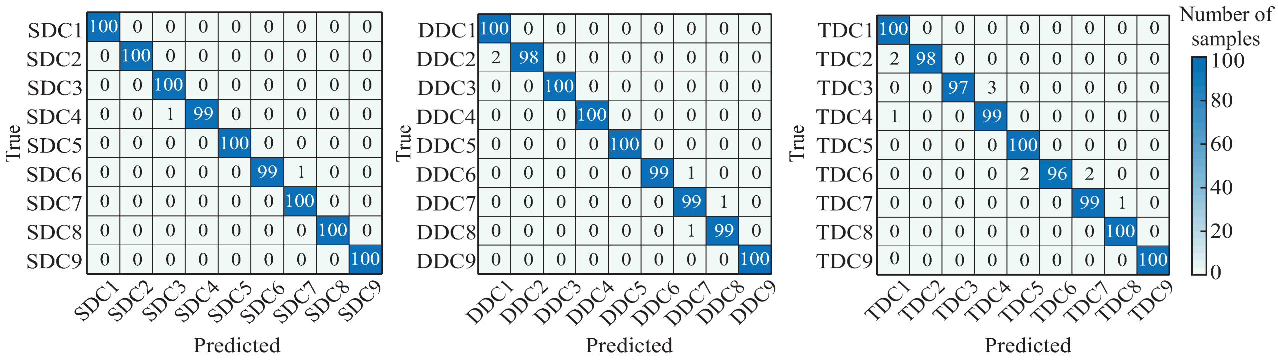

	SDC1	SDC2	SDC3	SDC4	SDC5	SDC6	SDC7	SDC8	SDC9
SDC1	100	0	0	0	0	0	0	0	0
SDC2	0	100	0	0	0	0	0	0	0
SDC3	0	0	100	0	0	0	0	0	0
SDC4	0	0	1	99	0	0	0	0	0
SDC5	0	0	0	0	100	0	0	0	0
SDC6	0	0	0	0	0	99	1	0	0
SDC7	0	0	0	0	0	0	100	0	0
SDC8	0	0	0	0	0	0	0	100	0
SDC9	0	0	0	0	0	0	0	0	100

(a)

	DDC1	DDC2	DDC3	DDC4	DDC5	DDC6	DDC7	DDC8	DDC9
DDC1	100	0	0	0	0	0	0	0	0
DDC2	2	98	0	0	0	0	0	0	0
DDC3	0	0	100	0	0	0	0	0	0
DDC4	0	0	0	100	0	0	0	0	0
DDC5	0	0	0	0	100	0	0	0	0
DDC6	0	0	0	0	0	99	1	0	0
DDC7	0	0	0	0	0	0	99	1	0
DDC8	0	0	0	0	0	0	1	99	0
DDC9	0	0	0	0	0	0	0	0	100

(b)

	TDC1	TDC2	TDC3	TDC4	TDC5	TDC6	TDC7	TDC8	TDC9
TDC1	100	0	0	0	0	0	0	0	0
TDC2	2	98	0	0	0	0	0	0	0
TDC3	0	0	97	3	0	0	0	0	0
TDC4	1	0	0	99	0	0	0	0	0
TDC5	0	0	0	0	100	0	0	0	0
TDC6	0	0	0	0	2	96	2	0	0
TDC7	0	0	0	0	0	0	99	1	0
TDC8	0	0	0	0	0	0	0	100	0
TDC9	0	0	0	0	0	0	0	0	100

(c)

Fig. 11 Structural damage identification results. (a) Single damage condition; (b) Double damage condition; (c) Triple damage condition

Table 8 Reconstruction result of the structural damage degree identification task

Statistical metrics	SDC		DDC		TDC	
	R^2	NRMSE	R^2	NRMSE	R^2	NRMSE
Best	0.993	9.51E−03	0.987	1.37E−02	0.984	1.48E−02
Average	0.971	1.36E−02	0.956	1.93E−02	0.949	2.10E−02
SD	3.46E−02	2.08E−03	5.28E−02	1.91E−03	5.15E−02	2.90E−03

Comparative analysis reveals that for the triple-damage scenario, the identification of structural damage severity and data compression/reconstruction results showed some fluctuations. Nevertheless, the model maintained high classification and reconstruction accuracy overall. This phenomenon primarily stems from the deeper damage coupling effects in the triple-damage scenario. These effects generate stronger variational interference in the dynamic characteristics of the scaled model and consequently impose more demanding requirements on the model's feature extraction capability.

4.3 Comparative analysis of model training efficiency

To quantify the improvement in the model convergence rate achieved by the gradient coupling joint mechanism, comparative experiments were conducted using the DDC condition dataset. As shown in Fig. 12, compared with the traditional two-stage training model (training duration: 82.66 min/2 836 iterations), GCAF demonstrates significant advantages in terms of the convergence efficiency: the training duration and iteration count are reduced to 37.66 min and 1 545 iterations, representing reductions of 54.4% and 45.5%, respectively. These improvements stem from optimization of the parameter update paths through the gradient coupling strategy.

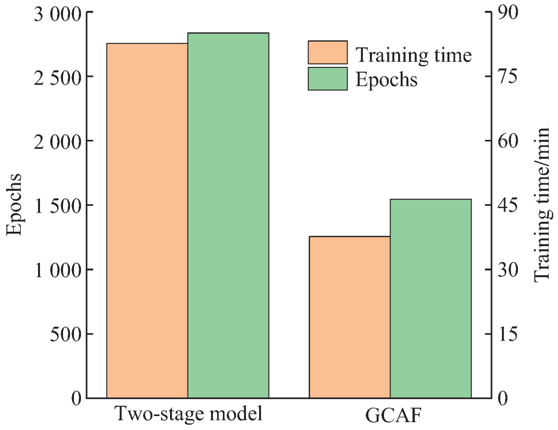

Fig. 12 Training time and epochs for different models

The two-stage model freezes the FCNN during the first training phase to focus on training the autoencoder for data reconstruction, then fixes the autoencoder parameters in the second phase to concentrate on FCNN classification tasks. In contrast, GCAF optimizes the parameter convergence process through dynamic gradient coupling of dual-task parallel training, thereby achieving accelerated training.

5 Conclusions

The GCAF proposed in this study balances the training process between data reconstruction and damage identification by coupling the parameter update gradients of dual tasks, thereby reducing the training time and optimizing parameter convergence.

(1) The proposed GCAF with ANAL maintains a reconstruction accuracy of R^2 = 0.916 and NRMSE = 0.028 8 even with the loss of 40% of the sensor nodes, while demonstrating robust performance (R^2 = 0.910, NRMSE = 0.025 3) under high noise levels (SNR = 12 dB).

(2) In the spatial localization of structural damage and severity identification tasks, GCAF achieves over 99.3% accuracy. This not only demonstrates the model's superior capability for decoupling damage condition data but also confirms the rationality and precision of the experimental design and model architecture.

(3) The unique GCM of GCAF significantly accelerates the convergence of the model parameters during training. Compared with traditional two-stage model training, GCM reduces the training duration and iteration counts by 54.4% and 45.5%, respectively.

References

[1] GHAREHBAGHI V R, NOROOZINEJAD F E, NOORI M, et al. A critical review on structural health monitoring: Definitions, methods, and perspectives[J]. Archives of Computational Methods in Engineering, 2022, 29(4): 2209-2235.

[2] SUN L M, SHANG Z Q, XIA Y, et al. Review of bridge structural health monitoring aided by big data and artificial intelligence: From condition assessment to damage detection[J]. Journal of Structural Engineering, 2020, 146(5): 04020073.

[3] SHAN J Z, ZHANG X, LOONG C N, et al. Predictive maintenance and its applications in civil engineering structures: A review[J]. Journal of Southeast University (English Edition), 2024, 40(3): 245-256.

[4] HU S Y, XIE Z N, YANG Y. Interference wind pressure prediction of high-rise buildings with square section based on machine learning[J]. Journal of Southeast University (Natural Science Edition), 2024, 54(6): 1425-1437. (in Chinese)

［5］ CHEN H，ZHU Y K，LEI B，et al. Sensor fault self-detection based on the mean shift method［J］. Journal of Southeast University（English Edition），2024，40（2）：140-147.

［6］ LIU F P. Study on the application of structural health monitoring system for Dongying Yellow River Bridge［J］. Qinghai Science and Technology of Transportation，2024，36(2)：141-146.（in Chinese）

［7］ YU B，QIU H X，WANG H，et al. Health monitoring system for Sutong Yangtze River Bridge［J］. Journal of Earthquake Earthquake Engineering and Engineering Vibration，2009，29(4)：170-177.（in Chinese）

［8］ LIU Z Q，LI N，GUO J，et al. Design and implementation of structural monitoring systems for Xihoumen Bridge（Ⅱ）：Implementations［J］. Engineering Sciences，2010，12(7)：101-106.（in Chinese）

［9］ ZHAO Z Q，ZHANG Y，HU J M，et al. Comparative study of PCA and ICA based traffic flow compression［J］. Journal of Highway and Transportation Research and Development，2008，25（11）：109-113，118.（in Chinese）

［10］ ZHOU S W，LIN Y P，YE S T，et al. A wavelet data compression algorithm with memory-efficiency for wireless sensor network［J］. Journal of Computer Research and Development，2009，46（12）：2085-2092.（in Chinese）

［11］ QUER G，MASIERO R，PILLONETTO G，et al. Sensing，compression，and recovery for WSNs：Sparse signal modeling and monitoring framework［J］. IEEE Transactions on Wireless Communications，2012，11（10）：3447-3461.

［12］ DUAN Y F，DUAN Z T，ZHANG H M，et al. Bridge damage identification based on convolutional autoencoders and extreme gradient boosting trees［J］. Journal of Southeast University（English Edition），2024，40（3）：221-229.

［13］ LIU Z J，JIN M R，ZHOU L C，et al. Bridge damage identification method based on structural response vectors and support vector machine algorithms［J］. Journal of University of Jinan（Science and Technology），2020，34(2)：106-112.（in Chinese）

［14］ DAI L C，CAO W，YI S C，et al. Damage identification of concrete structure based on WPT-SVD and GA-BPNN［J］. Journal of Zhejiang University（Engineering Science），2023，57：100-110，132.（in Chinese）

［15］ YANG D H，SUN J Z，YI T H，et al. Early warning technology of long-span bridge bearing deterioration considering time lag effects of thermal-induced displacement［J］. Journal of Southeast University（Natural Science Edition），2024，55(2)：268-274.（in Chinese）

［16］ SHAN D S，SHI L，TAN K X. Bridge damage identification based on CNN and LSTM deep network［J］. Bridge Construction，2023，53(4)：41-46.（in Chinese）

［17］ ZHANG C W，CHUN Q，MA Y K，et al. Research on damage detection of ancient stone arch bridges based on spatio-temporal difference graph convolutional neural network［J］. Journal of Southeast University（Natural Science Edition），2025，55(2)：370-379.（in Chinese）

［18］ ZHANG H M，HU F，DUAN Y F，et al. A vision-based deformation tracking for self-centering structures during shaking table tests［J］. Engineering Structures，2025，330：119800.

［19］ CHEN H，LI J B，YIN X G. A new experimental method for structural damage identification［J］. Journal of Experimental Mechanics，2011，26（1）：96-102.（in Chinese）

基于梯度耦合自编码器与全连接网络的桥梁传感器数据重构与结构损伤识别

段元锋，丁芃尧，段政腾，郑荣俊

（浙江大学建筑工程学院，杭州 310058）

摘要：为了提升桥梁传感器数据压缩编码的效率与任务适配性，提出了一种双任务并行机器学习框架。该框架由一个卷积自编码器（CAE）和一个全连接神经网络（FCNN）组成，利用梯度耦合机制（GCM）实现高效并行的数据压缩重构与损伤识别。该框架在一座三跨连续梁桥缩尺模型上进行了实验验证。实验结果表明，在传感器网络40%节点缺失的情况下，模型仍能取得R^2为0.916、NRMSE为0.028 8的全传感器网络重构效果；在SNR为12 dB的高噪声水平影响下，模型仍取得R^2为0.910、NRMSE为0.025 3的重构效果；在结构损伤空间定位与损伤程度识别的46个工况中，模型均取得了99.3%以上的识别精度。此外，模型训练时长与训练迭代次数相较于传统两阶段机器学习框架降幅分别达54.4%和45.5%。

关键词：结构健康监测；机器学习；数据压缩；损伤识别；卷积神经网络；全连接神经网络；梯度耦合机制

中图分类号：TU317.1